

Regioselective Friedel–Crafts Acylation Reaction Using Single Crystalline and Ultrathin Nanosheet Assembly of Scrutinyite-SnO₂

Sudakhina Saikia, Rasna Devi, Pranjal Gogoi, Lakshi Saikia, Boyapati M. Choudary, Thirumalaiswamy Raja, Pangkita Deka,* and Ramesh C. Deka*



Cite This: *ACS Omega* 2022, 7, 32225–32237



Read Online

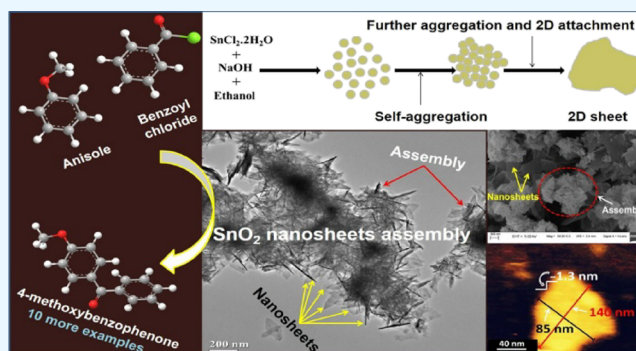
ACCESS |

Metrics & More

Article Recommendations

Supporting Information

ABSTRACT: Peculiar physicochemical properties of two-dimensional (2D) nanomaterials have attracted research interest in developing new synthetic technology and exploring their potential applications in the field of catalysis. Moreover, ultrathin metal oxide nanosheets with atomic thickness exhibit abnormal surficial properties because of the unique 2D confinement effect. In this work, we present a facile and general approach for the synthesis of single crystalline and ultrathin 2D nanosheets assembly of scrutinyite-SnO₂ through a simple solvothermal method. The structural and compositional characterization using X-ray diffraction (Rietveld refinement analysis), high-resolution transmission electron microscopy, atomic force microscopy, X-ray photoelectron spectroscopy, and so on reveal that the synthesized 2D nanosheets are ultrathin and single crystallized in the scrutinyite-SnO₂ phase with high purity. The ultrathin SnO₂ nanosheets show predominant growth in the [011] direction on the main surface having a thickness of ca. 1.3 nm. The SnO₂ nanosheets are further employed for the regioselective Friedel–Crafts acylation to synthesize aromatic ketones that have potential significance in chemical industry as synthetic intermediates of pharmaceuticals and fine chemicals. A series of aromatic substrates acylated over the SnO₂ nanosheets have afforded the corresponding aromatic ketones with up to 92% yield under solvent-free conditions. Comprehensive catalytic investigations display the SnO₂ nanosheet assembly as a better catalytic material compared to the heterogeneous metal oxide catalysts used so far in the view of its activity and reusability in solvent-free reaction conditions.



INTRODUCTION

Ultrathin two-dimensional (2D) nanomaterials are a class of material endowed with sheetlike nanostructure of atomic thicknesses and high area/thickness aspect ratios.^{1–10} Owing to the geometric confinement in one of the dimensions, they have been attracting a lot of attention as a new generation advanced material with distinctive physical/chemical properties.^{1–15} These compelling physical/chemical properties of 2D nanomaterials compared to bulk counterparts improve their applicability in various fields of catalysis, nanomechanics, gas sensors, and so on.^{2–20} Particularly, the ultrathin nanosheets are most versatile one as nearly all the active atoms of the material lie at the surface of nanosheets maximizing the utility of such atoms.^{2–25} Hence, the interaction between the weakly coordinated active surface atoms of the nanosheets and reactant species and the distinctive electronic property arising from 2D effects of nanosheets can tremendously change the activity of ultrathin nanosheets compared to conventional nanosheets/nanostructures.^{1–4} The synthesis of ultrathin nanosheets from 2D graphene and graphene-type materials with layered structures that are bonded by weak van der Waals force are easy to prepare from their bulk structure.^{10–12}

However, achieving ultrathin nanosheets and their assembly of a structurally nonlayered material with high activity and structural stability is extremely difficult. Moreover, it is challenging to synthesize single crystalline ultrathin nanosheets and their assembly with high structural stability/durability.

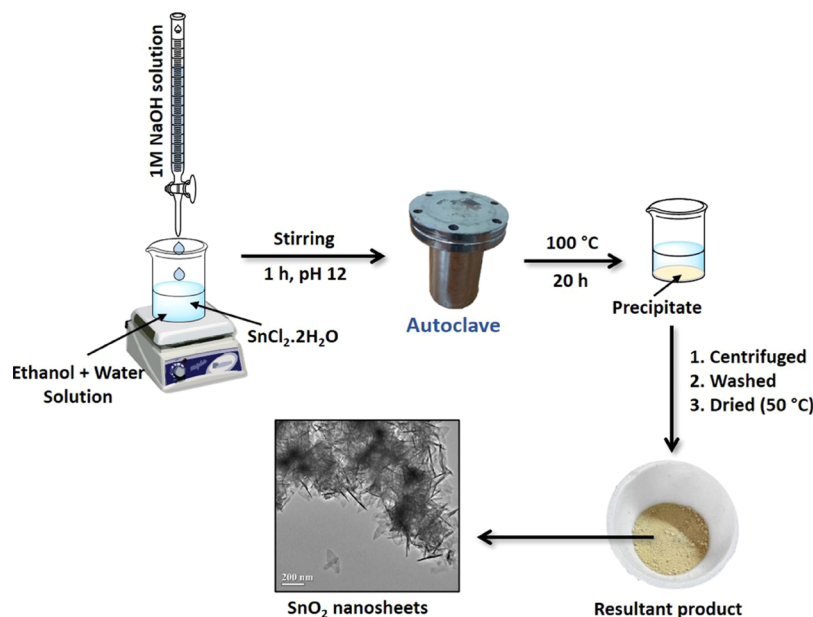
Recently, 2D ultrathin metal oxide (such as Co₃O₄, Rh₂O₃, ZnO, TiO₂, WO₃, SnO₂, and so forth) nanosheets with a microscopic level of thicknesses have been considered as advanced catalytic materials for heterogeneous catalytic reactions because of their improved catalytic activity and stability.^{26–29} Among the synthetically demanding 2D metal oxide nanomaterials, scrutinyite tin(IV) oxide with the orthorhombic crystal structure plays an important role in various applications because of its low electrical resistivity (10⁻⁴–10⁻³ Ω cm), high sensitivity to atmospheric gas

Received: June 7, 2022

Accepted: July 25, 2022

Published: August 31, 2022



Scheme 1. Schematic Representation of the Synthesis of Scrutinyite-SnO₂ Nanosheets

pollutants such as CO, CH₄, N_xO, and so forth, improved capacitance by combining with other phases, and so on.^{30–33} Normally, under ambient temperature and pressure, SnO₂ forms its most stable tetragonal rutile-type crystal phase.^{34–37} Conversely, the scrutinyite (α -PbO₂)-type orthorhombic crystal phase is known to be stable only at high pressures and temperatures.^{30,31} Still, a number of researchers have also claimed the formation of this crystal phase under ambient conditions. Moreover, scrutinyite-SnO₂ with an orthorhombic crystal structure exhibits unique physiochemical properties compared to the stable tetragonal rutile-type phase that also motivate researchers to develop easy synthetic routes to obtain this phase.^{30–33} However, because of stability concerns, the scrutinyite-SnO₂ phase is seldom investigated and reported in the past few years. As a result, the formation of stable scrutinyite-SnO₂ with the orthorhombic crystal structure under ambient conditions allows the exploration of new physical and chemical properties, opening its many possibilities for different applications.

The synthesis of the scrutinyite-SnO₂ phase is mainly related to the method used and the experimental conditions such as temperature, pressure, and so forth.^{31–33} Therefore, synthetic routes such as chemical vapor deposition, pulsed laser deposition, coprecipitation method, sol–gel method, and so forth are used so far. For example, epitaxial tin oxide film of the orthorhombic phase has been prepared by Kong et al. using the metal organic chemical vapor deposition (MOCVD) method.³⁸ Lamelas and Reid synthesized SnO₂ nanoparticles of the orthorhombic crystal phase by the oxidation and postheating treatment of mechanically milled SnO powder.³⁹ A sequence of orthorhombic SnO₂ thin films was also prepared by Chen et al. using pulsed laser deposition (PLD).⁵⁰ Carvalho et al. also observed the orthorhombic SnO₂ phase in a composite of (Sn_{1-x}Ce_x)O₂ synthesized using the sol–gel route.³³ Thus, all the above results indicate that the scrutinyite-type phase of orthorhombic SnO₂ can be easily synthesized using various experimental methods. It is reasonable to use high pressures and/or temperatures or strain as these factors can be vital for the formation of the orthorhombic phase of SnO₂.^{30–32}

However, till date, the use of solvothermal methods to prepare the orthorhombic phase of SnO₂ has been rarely reported. Besides the innumerable importance of the α -PbO₂-type phase of orthorhombic SnO₂, morphology-controlled synthesis of the orthorhombic SnO₂ nanostructure is scarce in reports. Furthermore, solvothermal synthesis and applications of single crystalline 2D ultrathin nanosheet or nanosheet assembly of scrutinyite-SnO₂ with an orthorhombic crystal structure have not been reported yet.

Again, the Friedel–Crafts (FC) acylation of aromatic substrates with acid halides is a fundamental and important conversion in organic synthesis.^{40–42} In particular, regioselective FC acylation to synthesize aromatic ketones have potential significance in chemical industry as the ketones are involved in the preparation of various synthetic intermediates,⁴³ chemical feedstocks,⁴⁴ pharmaceuticals,⁴⁵ and fine chemicals.⁴⁶ Although the aromatic ketones have tremendous applications, yet conventional strategies to produce such ketones often suffer from major challenges of complicated synthetic procedures and environmental concerns.^{47,48} The use of homogeneous catalysts, for example, protic acids,⁴⁹ soluble metal halides,⁵⁰ and substituted anhydrides⁵¹ in stoichiometric amounts and other homogeneous catalysts, for example, Ln(OTf)₃-LiClO₄,⁵² LiClO₄-acyl anhydride complex,⁵³ (PhCN)₂PtCl₂/AgSbF₆,⁵⁴ Re-Br(CO)₅,⁵⁵ and so on in the catalytic amount spectacle certain progress in the reaction. However, the industrial application of these homogeneous catalysts is also associated with various shortcomings because of the noneconomical reaction process and environmental issues.^{55,56} Therefore, design and development of a highly reactive and economical catalyst system with less environmental disputes is quiet challenging. Consequently, the effort has been focused on the synthesis of solid acid catalysts as certain surface properties of solids are not duplicated either in the solution or gas phase.⁵⁷ Various solid acid catalysts such as sulfated ZrO₂ or Fe₂O₃,^{58,59} sulfated Al₂O₃-ZrO₂ (or TiO₂),^{60,61} acidic zeolite,⁶² clays,⁶³ metal oxides,⁶⁴ heteropolyacid salts,⁶⁵ Nafion⁶⁶ and so forth have been used so far. Among them, mainly, the metal oxides have plenty of edge and

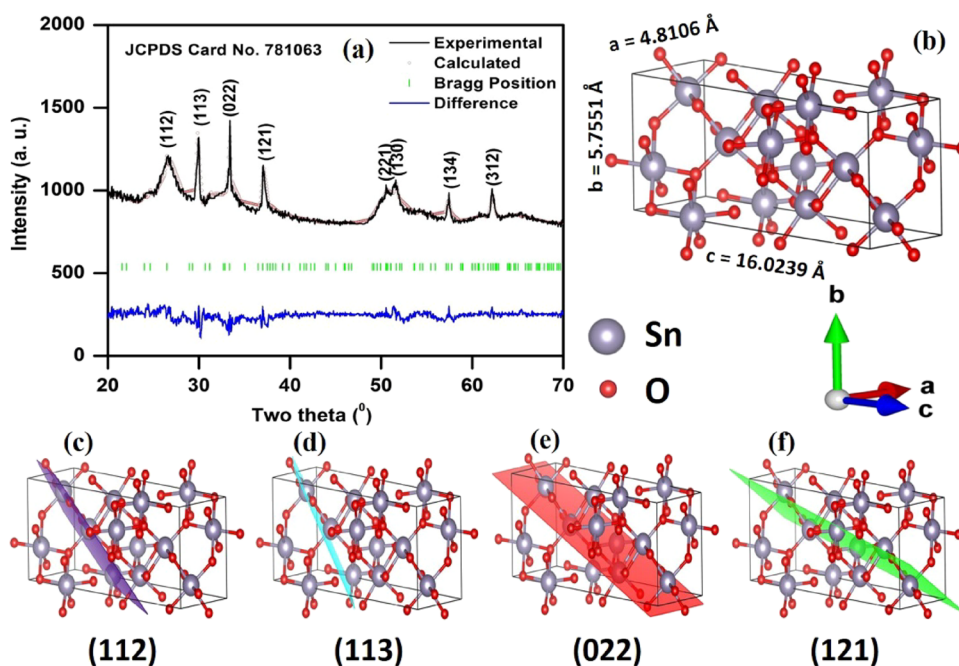


Figure 1. Results of the Rietveld refinement of the XRD pattern (a), corresponding unit cell (b), and crystallographic planes (c–f) of the scrutinyite-SnO₂.

corner sites for adsorption and activation of reactant molecules and are easily accessible, economically viable, and noncorrosive in nature.⁶⁷ At the present time, researchers have paid attention for synthesis and application of nanoscale metal or metal oxide catalysts for various organic transformations as catalysts in their nanometric regime provide improved reactivity and selectivity.^{68,69} However, use of metal oxide catalysts for regioselective FC acylation in their nanoscale dimension is extremely less in earlier reports.

Accordingly, herein, we have demonstrated an easy route to directly synthesize single crystalline 2D ultrathin scrutinyite-SnO₂ nanosheet assembly via a solvothermal method without using any external structure directing agent. Later, the single crystalline and ultrathin SnO₂ nanosheet assembly is used for the regioselective FC acylation of aromatic substrates in solvent-free conditions. Finally, the synthesized scrutinyite-SnO₂ nanosheets is represented as a better catalytic material compared to the conventional catalyst and heterogeneous catalysts used so far in the view of its activity/stability, reusability, and so forth.

EXPERIMENTAL SECTION

Synthesis of Scrutinyite-SnO₂ Nanosheets. In a typical synthesis of scrutinyite tin(IV) oxide, 22.5 g/L of SnCl₂·2H₂O is dissolved in a mixture of distilled water and ethanol (1:3) to form a homogeneous solution. The pH of the solution is maintained at 12 by adding NaOH solution (1 M) to the solution and stirred for 1 h. The final mixture is transferred to a Teflon-lined autoclave, which is sealed and heated to 100 °C for 20 h. After the autoclave is cooled, the resulting precipitate is separated by centrifugation, washed several times, and finally dried overnight in an oven at 50 °C. [Scheme 1](#) illustrates the procedure for the synthesis of scrutinyite-SnO₂ nanosheets.

Characterization. The synthesized SnO₂ nanosheets are characterized by Fourier transform infrared spectroscopy (FTIR), powder X-ray diffraction (p-XRD), scanning electron microscopy (SEM), field emission scanning electron micro-

scopy (FESEM), energy-dispersive X-ray (EDX) spectroscopy, transmission electron microscopy (TEM), atomic force microscopy (AFM), Raman spectroscopy, Brunauer–Emmett–Teller (BET) specific surface area analysis, X-ray photoelectron spectroscopy (XPS), temperature-programmed desorption of ammonia (NH₃-TPD) analysis, and FTIR spectroscopy of adsorbed pyridine (Py-FTIR). The products of the FC acylation reaction are characterized by ¹H and ¹³C nuclear magnetic resonance (NMR) spectroscopy and high-resolution mass spectrometry (HRMS). Further details on the characterization techniques are provided in the [Supporting Information](#).

Catalytic Experiments. The catalytic reaction is carried out in a 50 mL round-bottom flask equipped with a digital magnetic stirrer and a spiral glass condenser, immersed in a constant temperature oil bath. In this procedure, 10 mol % of catalyst and acid chloride (2 mmol) are mixed, followed by the addition of the aromatic substrate (4 mmol) to the mixture. The whole mixture is stirred at a desired temperature for a certain period of time until the reaction is complete (monitored by TLC). The reaction mixture is diluted with DCM, and the catalyst is separated from the reaction mixture by filtration. The DCM extract is washed with aqueous solution of sodium bicarbonate, and the organic layer is dried over anhydrous sodium sulfate. After solvent evaporation under reduced pressure, the product is purified by column chromatography. The isolated compound is identified and confirmed by different spectral analyses.

RESULTS AND DISCUSSION

Characterization of SnO₂ Nanosheets. Single crystalline and ultrathin nanosheets of scrutinyite-SnO₂ have been synthesized using a single-step solvothermal route at 100 °C for 20 h using ethanol as a typical solvent. At first, the FTIR spectroscopic study of the as-synthesized sample confirms the formation of metal oxide with strong absorption bands located at mid and far regions of IR spectra ([Figure S1](#)). The mid-

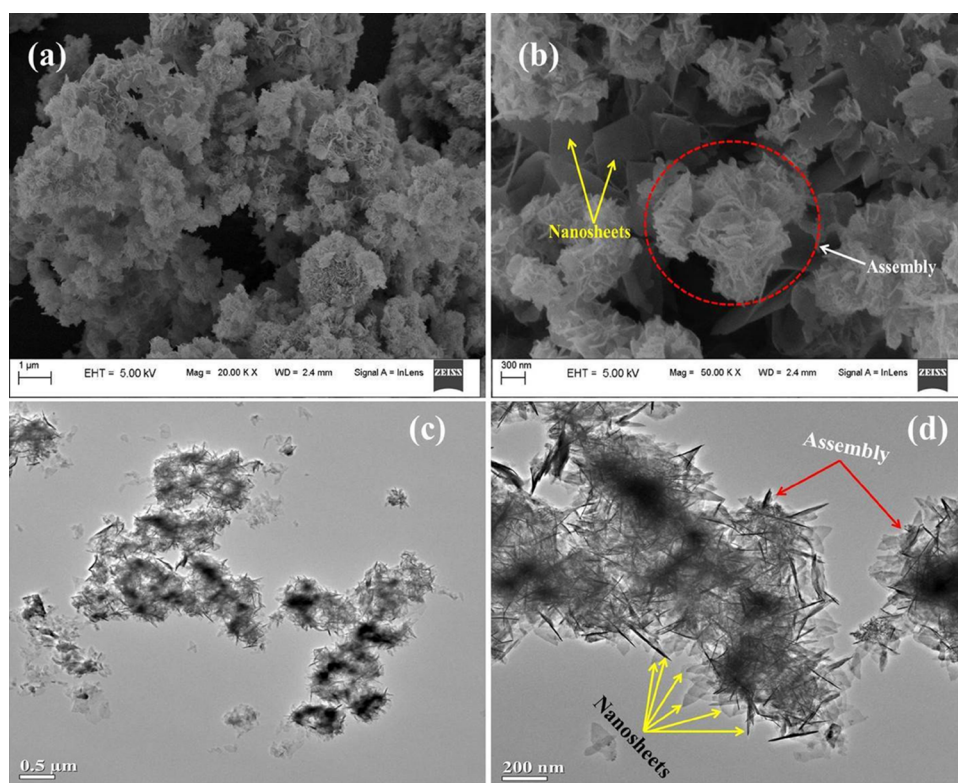


Figure 2. FESEM (a, b) and low-magnified TEM (c, d) images of synthesized scrutinyite-SnO₂ in different resolutions.

FTIR spectrum (Figure S1a) shows three intense bands at around 540.2, 585.6, and 692.0 cm^{-1} because of the stretching and bending vibration of Sn–O bonds in the orthorhombic SnO₂ lattice. The presence of a broad band at 3415.1 cm^{-1} and a weak band at 1643.2 cm^{-1} may be due to the stretching and bending vibration of hydroxyl groups of Sn–OH or coordinated H₂O molecules of the SnO₂ lattice.⁸ In the far-FTIR spectrum (Figure S1b), some weaker broad bands located around 150–300 cm^{-1} are observed that may be due to a few combination modes of bending and torsional vibrations of Sn–O bonds.⁷ No other absorption and inverse absorption bands are observed in the spectrum, indicating the absence of defects associated with oxygen vacancies or tin interstitials and molecular SnCl₂, respectively.⁸ Thus, this FTIR study confirms the formation of SnO₂ through the solvothermal treatment of tin chloride dihydrate with NaOH.

The powder XRD analysis is carried out for the as-synthesized sample, and results show the X-ray diffraction peaks at $2\theta = 26.9, 29.7, 33.4, 37.2, 47.2, 50.4, 51.8, 57.1, 60.8, 62.0, 65.3, 70.1, \text{ and } 78.1^\circ$ that are assigned to diffractions of (112), (113), (022), (121), (117), (221), (130), (134), (208), (312), (233), (228), and (240) crystal planes, respectively, of orthorhombic, that is, the scrutinyite-SnO₂ crystal structure correctly matches with JCPDS Card No. 78-1063 (Figure 1a). Rietveld refinements (Figure 1a) are also carried out using the same powder XRD data and found that all the diffraction peaks are indexed to the orthorhombic (scrutinyite) crystal phase of SnO₂ with space group Pbcn (No. 60). Table S1 represents all the lattice and structure parameters of the scrutinyite-SnO₂ sample. There are no oxygen vacancies in the SnO₂ sample, confirming the complete formation of scrutinyite-Sn(IV)O.⁷

Again, the crystallite size of the SnO₂ sample is calculated considering the full width at half-maximum (FWHM) of the first four high intense XRD peaks at $2\theta = 26.9, 29.7, 33.4, \text{ and}$

37.2° corresponding to (112), (113), (022), and (121) crystal planes. The crystallite sizes of the (112), (113), (022), and (121) planes of the as-synthesized SnO₂ sample are found to be 12.2, 26.9, 71.2, and 23.8 nm, respectively. The crystallite size of the (022) plane is found to be much larger than that of the other planes, suggesting the main growth of as-synthesized SnO₂ crystallites in the [011] direction. The result means the main surface of the SnO₂ sample is predominantly contributed by the (022) plane or/and parallel planes in the [011] direction. Consequently, the growth of crystallites of the SnO₂ sample perpendicular to the [011] direction, that is, in the [100] direction, must be slow. This means that the planes in the [100] direction or/and the parallel planes of the (100) plane have minor contribution to the main surface of SnO₂ sample.

The morphology and structural/compositional details of the synthesized scrutinyite-SnO₂ have been studied by SEM/FESEM and TEM analyses. SEM images (Figure S1c,d), FESEM images (Figure 2a,b), and TEM images (Figure 2c,d) confirm the formation of SnO₂ nanosheets and assembly of such nanosheets with almost dendritic-like morphology. More information about the SnO₂ nanosheets and its assembly is collected by a series of TEM/HRTEM investigations (Figure 3a–h). The size of the SnO₂ nanosheets is found to be nonuniform with longitudinal dimensions of almost 120–200 nm and lateral dimensions of 50–100 nm (Figure 3a). The thickness, that is, cross-sectional dimension of SnO₂ nanosheets is determined by focusing TEM/HRTEM investigation on the edge of the nanosheet assembly. The completely transparent fringelike regions indicate planar sheets parallel to copper grid, and quite dark wirelike regions resemble the sheets perpendicular to the grid (Figure 3b). The measured widths of very dark wirelike regions are found to be 1.2–1.35 nm that confirms the formation of ultrathin nanosheets (Figure

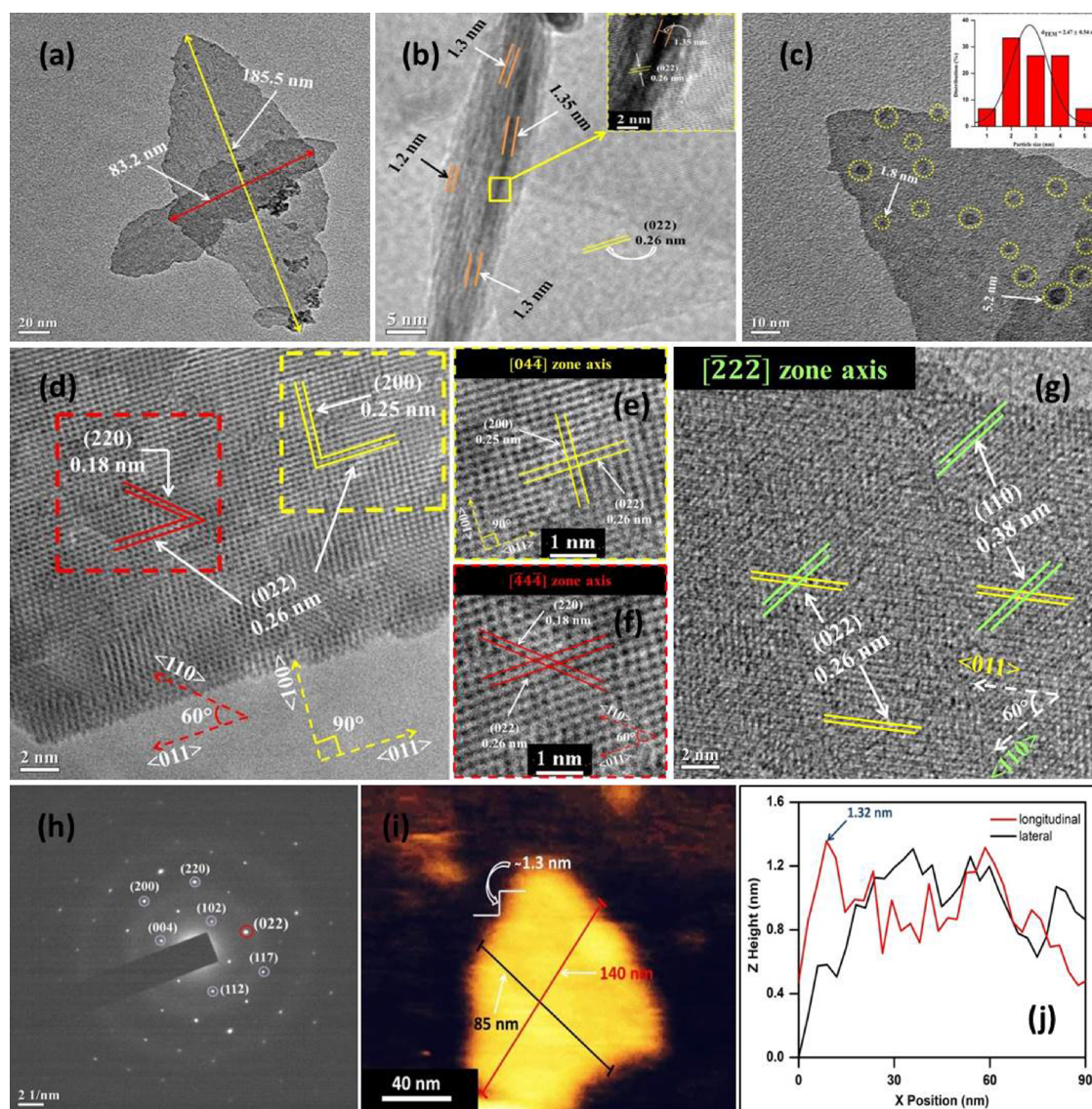


Figure 3. Morphological and topological characterizations for scrutinyite-SnO₂ nanosheet assembly. Low-magnification TEM image (a) representing nanosheets, HRTEM image (b) of nanosheet assembly on the edge region (inset shows high magnified image of the yellow square box portion), low-magnification TEM image (c) of a portion of the nanosheet displaying the aggregation and attachment of tiny particles (slightly visible on the top flat surface of the sheet) (the inset shows the corresponding particle size distribution), HRTEM image (d) of a nanosheet having two different zonal area (yellow and red square box corresponding to [044] and [444] zone axes, respectively), high magnified HRTEM image of yellow color square box corresponding to [044] (e) and red color square box corresponding to the [444] (f) zone axis, HRTEM image (g) of a different portion of the nanosheet displaying [222] zone axis, SAED analysis (h) of the nanosheet, AFM image (i) of the SnO₂ nanosheet after strong ultrasonic treatment, corresponding height profiles (j) from the AFM analysis of the SnO₂ nanosheet.

3b). The planar sheet also clearly displays lattice fringes with a spacing of 0.26 nm corresponding to the (022) plane of scrutinyite-SnO₂ (Figure 3b). Again, a particularly magnified area of the HRTEM image distinctively shows the lattice fringes ($d_{022}^{\text{SnO}_2} = 0.26$ nm) over the planar nanosheet of scrutinyite-SnO₂ (inset in Figure 3b). Moreover, the nanosheets are formed by strong aggregation and oriented attachment of various tiny particles of a few nanodiameters (slightly visible on the top flat surface of the sheet) (Figure 3c). The average diameter of the particles is calculated and found ca. 2.47 nm (inset in Figure 3c).

As of yet, the assembly of scrutinyite-SnO₂ formed by ultrathin nanosheets that are made of oriented attachment of tiny particles have been found under TEM/HRTEM investigation. Thereafter, the high-resolution TEM investiga-

tion is performed for the collection of in-depth information on SnO₂ nanosheets (Figure 3d–g). Two different zonal areas highlighted with yellow and red color square box corresponding to [044] and [444] zone axis are observed on the surface of a nanosheet (Figure 3d–f). A distinctive set of planes matching with (022) and (200) lattice planes of scrutinyite-SnO₂ at an angle of 90° in between having lattice fringes ($d_{022}^{\text{SnO}_2} = 0.26$ nm) and ($d_{200}^{\text{SnO}_2} = 0.25$ nm), respectively, in the [044] zone axis is clearly visible (highlighted yellow color square box of Figure 3d,e). Another set of plane matching with (022) and (220) lattice planes of scrutinyite-SnO₂ making an angle of 60° in between with fringes ($d_{022}^{\text{SnO}_2} = 0.26$ nm) and ($d_{220}^{\text{SnO}_2} = 0.18$ nm), respectively, in the [444] zone axis is also observed (highlighted red color square box of Figure 3d,f). Another zonal area with a set of planes matching with the (022) and

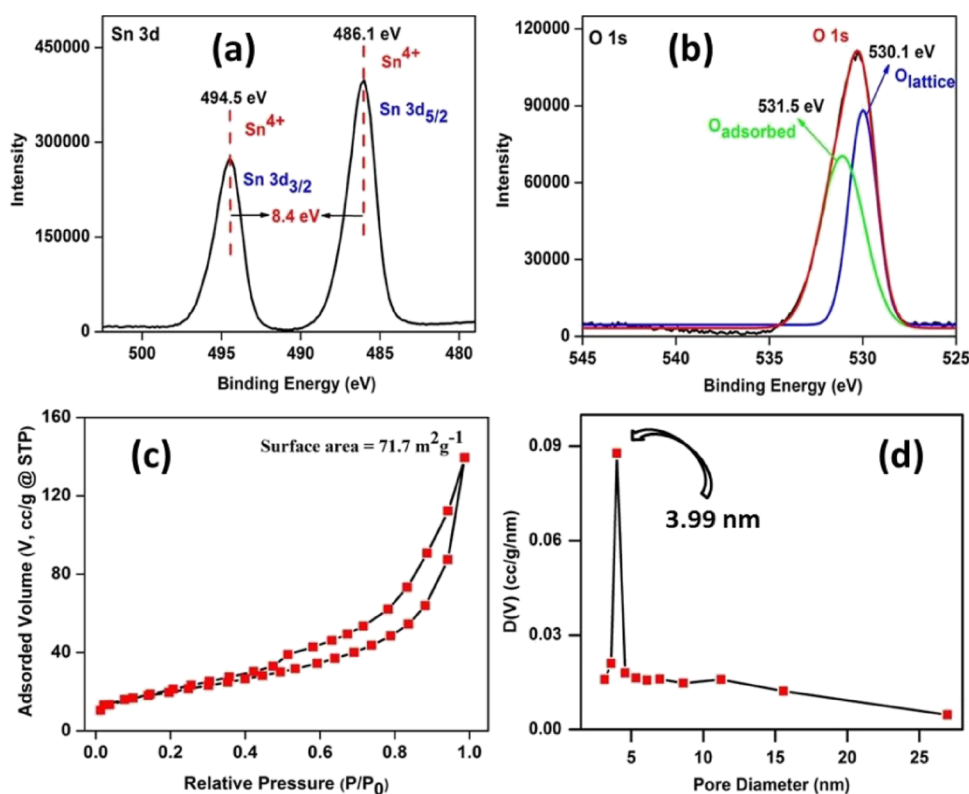


Figure 4. XPS spectrum of Sn 3d (a) and O 1s (b), BET isotherm (c), and pore size distribution (d) of the scrutinyite-SnO₂ nanosheet assembly.

(110) lattice planes of scrutinyite-SnO₂ at an angle of 60° in between having lattice fringes ($d_{022}^{\text{SnO}_2} = 0.26$ nm) and ($d_{110}^{\text{SnO}_2} = 0.38$ nm), respectively, is also viewed in the $[2\bar{2}2]$ zone axis of a different portion of the nanosheet (Figure 3g).

From the HRTEM investigation, the lattice plane (022) corresponding to the {022} facet of scrutinyite-SnO₂ ($d_{022}^{\text{SnO}_2} = 0.26$ nm) in the [011] direction predominantly contributed to the main surface of the nanosheets along with two other exposed planes (220) and (110) in the [110] direction at an angle of 60° to the (022) plane. Moreover, a lattice plane (200) corresponding to the {200} facet in the [100] direction at an angle of 90° to the (022) plane also contributes slightly. These results are consistent with the XRD results by confirming the (022) lattice plane as the main exposed crystal plane of the scrutinyite-SnO₂ nanosheets, suggesting predominant growth and orientation of the SnO₂ crystallites in the [011] direction with least contribution of the (200) lattice plane in the [100] direction. Furthermore, SAED analysis of the nanosheet shows a spotty pattern, revealing the pure and single crystalline nature of the synthesized SnO₂ nanosheets (Figure 3h). The lattice planes (004), (102), (112), (022), (220), (200), and (117) of scrutinyite-SnO₂ are clearly indexed by the bright spots in the SAED pattern. The higher brightness of the (022) spot (red color circle) in the pattern confirms more exposure of the (022) lattice plane in the SnO₂ nanosheets, and this is again in agreement with HRTEM and XRD observations. Again, the thickness of the SnO₂ nanosheet can be further characterized by AFM analysis (Figure 3i,j). The AFM image depicts a thickness ca. 1.3 nm along with longitudinal and lateral dimensions of the nanosheet about 140 and 85 nm, respectively (Figure 3i). The corresponding height profiles show slight roughness in the surface of the nanosheet with the height in the range of 0.7–1.32 nm and a

maximum height of ~1.32 nm (Figure 3j). The result of AFM analysis strongly confirms the formation of ultrathin nanosheets, which is in good agreement with the HRTEM observation.

Furthermore, we have conducted Raman spectroscopic and XPS analysis on the single crystalline and ultrathin SnO₂ nanosheet assembly (Figures S2 and 4). Basically, Raman spectroscopy is interrelated with XRD. However, in contrast to XRD, the number of atoms per unit cell provides the possible phonon modes in Raman spectroscopy. As the primitive cell of scrutinyite-SnO₂ contains 12 atoms, one should achieve a total of 33 normal modes of vibration. The vibrational representation of those optical phonon modes at the center of the Brillouin zone can be given by eq 1.

$$\Gamma = 4B_{1u} + 3B_{2u} + 4B_{3u} + 4A_g + 5B_{1g} + 4B_{2g} + 5B_{3g} + 4A_u \quad (1)$$

All of these nondegenerate vibrational modes are IR-active (B_{1u} , B_{2u} , and B_{3u}), Raman-active (A_g , B_{1g} , B_{2g} , and B_{3g}), and the A_u modes are silent. The vibrational modes on the spectrum do not match with the characteristic modes of tetragonal (rutile) and deformed rutile phases of SnO₂, which is in good agreement with the XRD results. However, till date, no spectral analysis for the Raman spectrum of SnO₂ in its orthorhombic (scrutinyite) phase has been reported yet. As there is scarce of data in the literature, it is difficult to completely assign the observed phonon modes. Therefore, we can confirm the formation of the orthorhombic phase of SnO₂ in resemblance with the Raman spectrum of the α -PbO₂ (scrutinyite) and metal oxides having a scrutinyite crystal structure.^{31–33} The XPS analysis is carried out to investigate the chemical state of the SnO₂ nanosheets (Figure 4a,b). The

Sn 3d XPS spectrum displays two peaks at binding energies 486.1 and 494.5 eV for Sn 3d_{5/2} and 3d_{3/2} states, respectively (Figure 4a). The binding energies are very close to the standard data for Sn⁴⁺, and no peaks either for Sn²⁺ or Sn⁰ is detected. The energy difference between Sn 3d_{5/2} and Sn 3d_{3/2} states of 8.4 eV is in agreement with the reported value of energy splitting for Sn(IV)O₂. Again, in the O 1s spectrum, two deconvoluted peaks located at binding energies 530.1 and 531.5 eV are observed (Figure 4b). The peak at 530.1 eV is ascribed to oxygen bound to Sn in the SnO₂ crystal lattice. Another peak located at 531.5 eV is attributed to the adsorbed oxygen (O⁻ and O²⁻) species (e.g., OH and H₂O), respectively. Finally, the XPS spectra indicate that the synthesized nanosheets are Sn(IV)O₂ rather than Sn(II)O or Sn(0) metals.^{8–10}

The nitrogen adsorption–desorption analysis is also performed to determine the specific surface area and pore size of the as-synthesized SnO₂ nanosheet assembly. A type IV isotherm characteristic of mesoporous material with hysteresis loop H3-type according to IUPAC is observed for the sample (Figure 4c). The BET surface area about to 71.7 m² g⁻¹ is found for the nanosheets, which is comparatively larger than the surface area of commercial SnO₂ powder (Sigma-Aldrich; 38.3 m² g⁻¹) and quite reasonable for SnO₂ nanomaterials.^{7–10} Again, the pore size distribution based on the BJH model is determined from the desorption branch of the isotherm. The BJH pore volume and diameter 0.21 cm³ g⁻¹ and 3.99 nm, respectively, is observed for the sample. The maximum of pore size distribution from the curve is observed at 3.99 nm, clearly indicating the mesoporosity of the sample (Figure 4d).

To evaluate the acidity of the synthesized SnO₂ nanosheets, the temperature-programmed desorption of ammonia (NH₃-TPD) is performed (Figure S3). The NH₃-TPD profile shows a broad desorption peak in the range 250–550 °C. In general, the strength of acidic sites can be divided into weak (200–300 °C), medium (300–450 °C), and high (>450 °C) regions.^{70,71} The measured NH₃-TPD profile is deconvoluted into three peaks having maximal temperatures at ~320, 361, and 446 °C corresponding to 23, 45, and 32% of the total desorbed amount of NH₃. All the peaks can be assigned to the medium temperature region (300–450 °C), which indicates the presence of medium strength acidic sites in the SnO₂ nanosheets.⁷² Moreover, the nature and stability of the acidic sites in the synthesized SnO₂ nanosheets are evaluated by performing Py-FTIR analysis at different temperatures, and the results are presented in Figure 5. The Py-FTIR spectra exhibit bands at 1610, 1575, and 1450 cm⁻¹ corresponding to the vibrational modes of pyridine coordinated at Lewis acidic sites (L). The two bands at 1610 and 1450 cm⁻¹ are characteristic of strong Lewis acidic site-bound pyridine, while another band at 1575 cm⁻¹ corresponds to weak Lewis acidic site-bound pyridine.⁷³ Again, the bands at 1650, 1540, and 1517 cm⁻¹ are attributable to pyridine molecules protonated at Bronsted acidic sites (B).^{74,75} Besides, another less-intense band at 1485 cm⁻¹ originates from pyridine associated with both Lewis and Bronsted acidic sites (L + B).⁷⁶ All the bands are thermally stable at 200 °C, which suggests that the acidic sites present in the nanosheets remain intact.

By following the experimental results, we can propose a reasonable mechanism for the formation of 2D SnO₂ nanosheets. The 2D SnO₂ nanosheets can be obtained by the solvothermal treatment of Sn(II) salts in alkaline aqueous solution in the presence of ethanol via hydrolysis, oxidation,

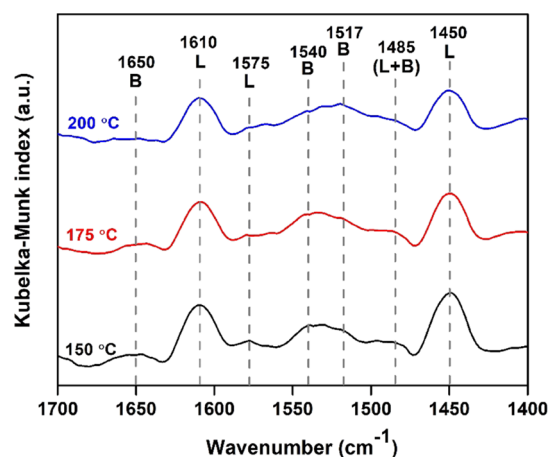
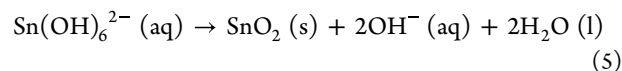
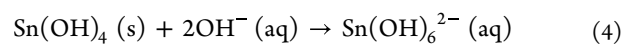
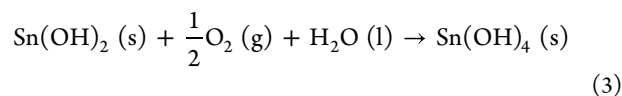
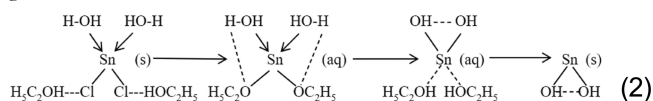


Figure 5. Py-FTIR spectra of synthesized SnO₂ nanosheet assembly at different temperatures.

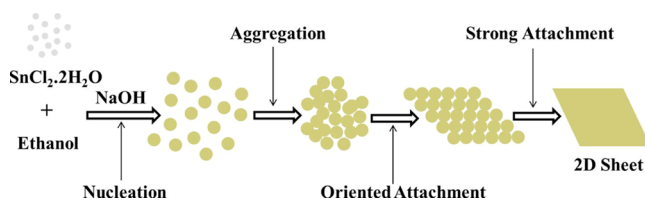
and decomposition of Sn(II) salts/ions.^{30–34} In general, the hydrolysis of Sn(II) salt may lead to the formation of layered/sheetlike hydroxide intermediates, which further oxidize and/or decompose to the sheetlike structure of SnO₂.^{7–10} Therefore, chemical reactions involved during the synthesis process can be described as follows:



As the solution is rich in ethanol, initially, Cl⁻ is replaced from SnCl₂·2H₂O molecules by C₂H₅OH (eq 2). Later, the H₂O molecules may attack the Sn-OC₂H₅ bonds and replace the C₂H₅OH molecules to form Sn(OH)₂ (eq 2). Subsequently, the Sn(OH)₂ may undergo oxidation to the precipitate as Sn(OH)₄ (eq 3). Afterward, the OH⁻ ion from the alkaline (NaOH) solution interacts with Sn(OH)₄ and forms Sn(OH)₆²⁻ (eq 4). Furthermore, the decomposition of Sn(OH)₆²⁻ may take place forming the crystals of SnO₂ (eq 5). Finally, the formation and self-construction mechanism of 2D SnO₂ nanosheets by oriented attachment from 0D nanocrystallites is schematically represented in Scheme 2.

Catalytic Activity of SnO₂ Nanosheets. Nanoscale metal oxides are less frequently employed for FC acylation reaction.

Scheme 2. Schematic Representation of the Formation and Self-Construction Mechanism of 2D SnO₂ Nanosheets (*l* ≈ 140 nm, *b* ≈ 85 nm, and *h* ≈ 1.32 nm)



Therefore, in the present study, we have performed the FC acylation reaction over as-synthesized single crystalline and ultrathin SnO₂ nanosheet assembly to evaluate its catalytic activity. To determine the standard experimental conditions, we have chosen the acylation reaction of anisole (aromatic substrate) and benzoyl chloride (acylating agent) as a model reaction. No product formation takes place without the catalyst in the reaction, suggesting the role of the catalyst (Table 1,

Table 1. Effect of the Solvent on the Acylation of Anisole with Benzoyl Chloride^a

entry	catalyst	solvent	time (min)	yield ^b (%)
1	none	solvent-free	>120	0
2	SnO ₂	acetonitrile	120	46
3	SnO ₂	nitromethane	120	45
4	SnO ₂	ethyl acetate	120	trace
5	SnO ₂	tetrahydrofuran	120	trace
6	SnO ₂	dichloromethane	120	59
7	SnO ₂	solvent-free	50	92

^aReaction Conditions: anisole (4 mmol), benzoyl chloride (2 mmol), solvent (0.5 mL), catalyst (10 mol %), and temperature (50 °C).
^bIsolated yield.

entry 1). As the temperature has a significant role on a reaction therefore at first, we have tested the reaction at different temperatures and observed that the yield of product 4-methoxybenzophenone (3a) is considerably affected by the reaction temperature (Figure S4). The increase in the reaction temperature from room temperature (=27 °C) to 50 °C enhanced the yield of the product from 46 to 92%, respectively, perhaps due to the higher molecular thermal agitation and collision probability between the benzoyl cation and the arene.⁷⁷ Further increase in the reaction temperature does not alter the yield of aromatic ketone. Thus, the reaction temperature 50 °C is considered as a prime temperature for the major yield of aromatic ketones in the presence of as-synthesized SnO₂ nanosheets.

To achieve maximum yield of the product, the reaction is optimized by changing the amount of the catalyst (Figure S5). The figure shows that as the amount of the catalyst increases the yield of the product of the reaction increases because of the increase in the concentration of the benzoyl cation that accelerates the reaction,⁷⁷ and a maximum yield of the product is observed with 10 mol % of the catalyst. No further improvement of the reaction yield is observed on employing more than 10 mol % SnO₂ nanocatalyst, presumably due to the fact that the reaction mixture becomes more viscous, leading to resistance in mass transfer. The observations suggest that a notable result is attained when the acylation reaction is carried out with 10 mol % of the SnO₂ nanocatalyst at 50 °C.

Moreover, the effect of the solvent on the entitled reaction is observed in the presence of five different solvents (Table 1). Although the reaction progress is smooth in the presence of solvents, miserable yields of the product are observed (Table 1, entries 2–6). A trace amount of the product is detected with solvents ethyl acetate and tetrahydrofuran having strong coordination ability (Table 1, entries 4 and 5).⁷⁸ In the same reaction, if carried out in nitromethane or acetonitrile, only 45 and 46% yields are detected, respectively. Noticeably, dichloromethane provides a better amount of product, yet less improvement (59% yield) is noticed (Table 1, entry 6). Meanwhile, the acylation of anisole is also performed under

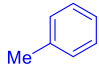
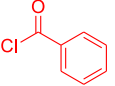
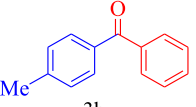
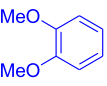
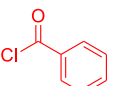
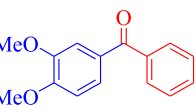
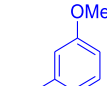
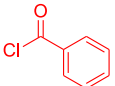
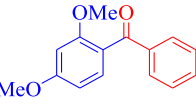
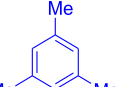
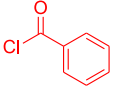
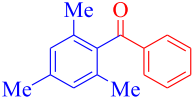
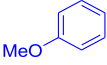
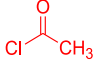
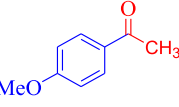
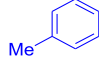
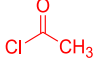
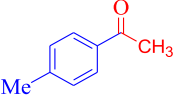

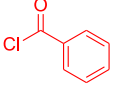
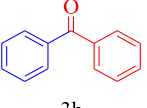

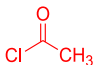
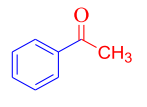

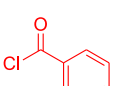
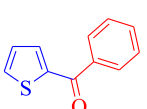
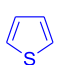
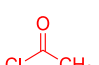
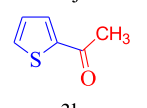
solvent-free conditions, resulting in a commendable yield of 92% (Table 1, entry 7). The observation suggests that there is no significant effect of solvents in the reaction, which is in agreement with literature reports, and a good result is obtained by employing aromatic ether as the self-solvent.⁷⁹

To explore the substrate scope of the reaction, a range of aromatic compounds and acid chlorides are reacted under optimized conditions, and the subsequent results are presented in Table 2. It is observed that acylation occurs exclusively at the position para to methoxy (–OCH₃) and methyl (–CH₃) groups for all the substituted aromatic compounds furnishing corresponding products within 40–70 min (Table 2, entries 1–6). The presence of electron-releasing –OCH₃ and –CH₃ groups in these cases resulted in good to high yields (78–92%) of corresponding aromatic ketones at 50 °C. However, the acylation of benzene (Table 2, entries 7 and 8) proceeds after vigorous stirring, affording low yields of corresponding products due to its low activity.⁸⁰ The reaction proceeds well with five-membered heterocyclic compounds such as thiophene (Table 2, entries 9 and 10), yielding quantitative amounts of 2-acylated products. The SnO₂ nanosheet assembly exhibits remarkable catalytic activity with excellent regioselectivity of aromatic ketones under solvent-free reaction conditions, which may be attributed to the ultrathin 2D confinement effect, acid site, and the redox behavior of the SnO₂ nanosheets.

Recyclability of the catalyst is a prime factor regarding environmental sustainability and economic industrial processes. To test the recyclability of the catalyst, six repeated cycles of catalytic reaction are performed and presented in Figure 6a. After each consecutive run, the catalyst is recovered from the reaction mixture followed by centrifugation, washing with ethanol, drying, activation, and redispersion in a freshly prepared identical reaction mixture. The high yield of aromatic ketone is retained without much loss of activity up to the sixth consecutive run, indicating the fair stability of the catalyst. The minute decrease in activity may be considered for the unavoidable mechanical loss of the catalyst during separation from every previous runs.

Moreover, a hot filtration test is conducted to investigate the leaching of the SnO₂ nanocatalyst (Figure 6b). After the first 10 min expedition of the model reaction between anisole and benzoyl chloride under optimized conditions, the catalyst is separated from the reaction mixture by simple filtration. The filtrated reaction mixture is further continued for additional 50 min. No obvious enhancement of the % conversion is noticed after separation of the catalyst, suggesting no significant leaching of the catalyst. After completion of the sixth run, the composition and morphology of the recovered SnO₂ nanocatalyst is studied by using FTIR, XRD, and TEM/HRTEM analyses. The FTIR spectrum of the recycled catalyst exhibited no significant changes, implying that the functionalities of the catalyst remained unchanged even after six consecutive runs (Figure S6). The powder XRD pattern of the reused catalyst also shows inconsequential changes than that of the fresh catalyst, confirming the good structural stability of the catalyst (Figure S7a). TEM investigation of the reused catalyst reveals that the nanosheets of the SnO₂ catalyst are very slightly broken and stacked compared to those of the fresh catalyst probably due to continuous stirring under heat (Figure S7b). However, the distinctly visible lattice fringes in the HRTEM images indicate that the crystallinity of the nanosheets is still intact in the recovered catalyst (inset in Figure S7b). The

Table 2. Substrate Scope for FC Acylation Reaction over SnO₂ Nanosheets^a

Entry	Substrate	Acid chloride	Product	Time (min)	Yield ^b (%)
1			 3b	70	84
2			 3c	60	86
3			 3d	50	80
4			 3e	40	78
5			 3f	50	87
6			 3g	60	83
7			 3h	>120	Trace
8			 3i	120	40
9			 3j	50	86
10			 3k	40	84

^aReaction Conditions: substrate (4 mmol), acid chloride (2 mmol), catalyst (10 mol %), and temperature (50 °C). ^bIsolated yield.

overall TEM observation confirms the high structural and morphological stability of the catalyst.

Proposed Reaction Mechanism for the FC Acylation over SnO₂ Nanosheets. The plausible mechanism involved for the action of SnO₂ nanosheets in acid-catalyzed FC acylation is shown in Scheme 3. FC acylation is an electrophilic aromatic substitution reaction, and the reaction is due to the generation

of an acyl carbonium ion. Mainly, acidic sites of the nanocatalyst facilitate the formation of the acylium ion. At first, adsorption of acid chloride takes place on the acidic site of the SnO₂ nanocatalyst that converts into acylium ions. This acylium ion acts as an electrophile and reacts with the nucleophilic aromatic substrate to generate the corresponding aromatic ketone.

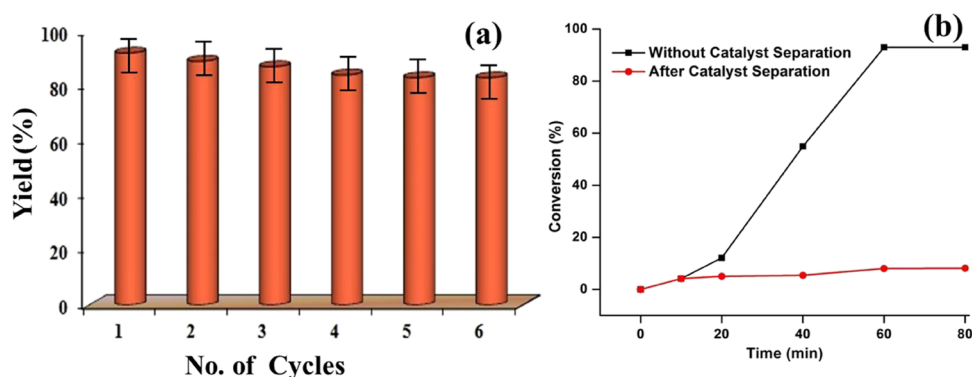
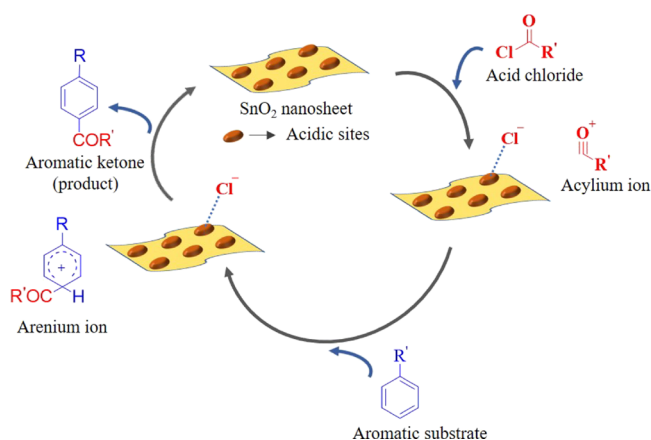
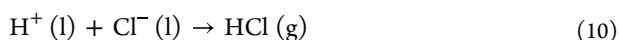
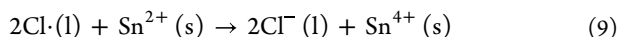
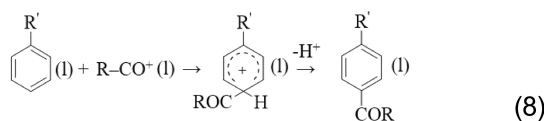
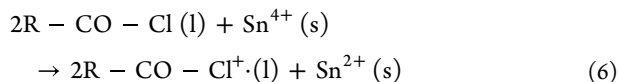


Figure 6. Recyclability test (a) and hot filtration test for leaching (b) of the SnO₂ nanocatalyst.

Scheme 3. Schematic Representation of the Acid-Catalyzed Mechanism of FC Acylation over SnO₂ Nanosheets (*l* ≈ 140 nm, *b* ≈ 85 nm, and *h* ≈ 1.32 nm)



Again, the reduction of Sn⁴⁺ to Sn²⁺ is relatively easy owing to the positive standard reduction potential for Sn⁴⁺ (aq) + 2e⁻ → Sn²⁺ (aq) ($E_{\text{Sn}^{4+}/\text{Sn}^{2+}}^{\circ} = +0.13$ V).⁸¹ Therefore, along with the conventional acid-catalyzed mechanism for FC acylation, a redox mechanism also can be expected.^{82,83} The steps involved in this pathway are mentioned below:



The acid chloride gets activated to 2R-CO-Cl⁺ with the reduction of Sn⁴⁺ to Sn²⁺ simultaneously (eq 6), thereby generating the R-CO⁺ carbocation (eq 7). Subsequently, the carbocation reacts with the aromatic substrate, resulting in the formation of the acylated product (eq 8). Furthermore, Sn²⁺ is oxidized back to Sn⁴⁺ (eq 9), followed by the liberation of HCl (eq 10).

Finally, we compared some results obtained in this work with that of other metal oxide catalysts, and the results are listed in Table 3. In the case of ZrO₂, Fe₂O₃, and Fe₂O₃/HY

Table 3. Comparative Study for FC Acylation of Aromatic Compounds with Benzoyl Chloride Using Different Metal Oxide Catalysts

entry	catalyst	substrate	conditions	time	yield (%)	refs
1	ZrO ₂	anisole	solvent-free/120 °C	5 h	65	84
2	Fe ₂ O ₃	anisole	solvent-free/80 °C	120 min	32	64
3	Fe ₂ O ₃ /HY	toluene	solvent-free/110 °C	10 h	43	85
4	PANI/nano-ZnO	anisole	solvent-free/rt	10 min	95	86
5	SnO ₂ -SiO ₂	anisole	CH ₃ NO ₂ /80 °C	30 min	86	87
6	TiO ₂	toluene	solvent-free/80 °C/MW	20 s	68	88
7	SnO ₂ nanosheets	anisole	solvent-free/50 °C	50 min	92	this work
8	SnO ₂ nanosheets	toluene	solvent-free/50 °C	60 min	84	this work

(Table 3, entries 1–3), although the reaction is performed in solvent-less conditions, it required prolonged time to furnish the products with comparatively lower yields than the present protocol. Although the results obtained with PANI/nano-ZnO and SnO₂-SiO₂ (Table 3, entries 4 and 5) are comparable to that of the present protocol, these methods require the preparation of the catalyst support.

The FC acylation of toluene with TiO₂ (Table 3, entry 6) completes quickly within 20 s. However, it requires higher reaction temperature (80 °C), microwave irradiation, and yields a lower amount (68%) of the corresponding product. These results clearly disclose that the synthesized SnO₂ nanosheets can be well utilized as an alternative for the regioselective acylation of aromatic compounds.

CONCLUSIONS

In summary, we have reported a facile and robust solvothermal route for the synthesis of single crystalline and ultrathin nanosheet assembly of SnO₂. The structural analyses have revealed that the SnO₂ nanosheets are ultrathin and single crystallized in the scrutinyite-SnO₂ phase with high purity. The ultrathin SnO₂ nanosheets have exposed preferential growth in the [011] direction on the main surface with a thickness of ca.

1.3 nm. Furthermore, the SnO₂ nanosheets have been employed for the regioselective FC acylation to synthesize aromatic ketones in solvent-free reaction conditions. The acylation reaction over the SnO₂ nanosheets afforded predominantly para-substituted ketones with yields up to 92% under mild reaction conditions. The comprehensive catalytic study has shown that the SnO₂ nanosheet assembly is a better catalytic material compared to other metal oxide catalysts used so far with respect to its activity and reproducibility. The 2D nanosheet assembly of scrutinyite-SnO₂ should be a highly promising catalyst for specific applications in the acylation reactions and will also open up some opportunities for the integration of various organic- and liquid-phase reactions.

■ ASSOCIATED CONTENT

SI Supporting Information

The Supporting Information is available free of charge at <https://pubs.acs.org/doi/10.1021/acsomega.2c03555>.

Materials; characterization techniques; lattice and structure parameters of scrutinyite-SnO₂; mid- and far-FTIR spectra; SEM images; Raman spectrum and TPD profile of SnO₂ nanosheets assembly; effect of temperature and catalyst dosage on the yield of 4-methoxybenzophenone; mid-FTIR spectrum; powder XRD and TEM image of recovered SnO₂ nanosheet assembly after six catalytic runs of FC acylation reaction; and analytical data and spectral copies of ¹H and ¹³C NMR of all the aromatic ketones (PDF)

■ AUTHOR INFORMATION

Corresponding Authors

Pangkita Deka – Department of Chemical Sciences, Tezpur University, Tezpur 784028, India; Department of Chemistry, Jorhat Engineering College, Jorhat 785007, India; Email: pangkitadeka@gmail.com

Ramesh C. Deka – Department of Chemical Sciences, Tezpur University, Tezpur 784028, India; orcid.org/0000-0003-4352-2661; Email: ramesh@tezu.ernet.in

Authors

Sudakhina Saikia – Department of Chemical Sciences, Tezpur University, Tezpur 784028, India

Rasna Devi – Department of Chemical Sciences, Tezpur University, Tezpur 784028, India

Pranjal Gogoi – Catalysis and Inorganic Chemistry Division, CSIR-National Chemical Laboratory, Pune 411008, India

Lakshi Saikia – Materials Sciences and Technology Division, CSIR-North East Institute of Science and Technology, Jorhat 785006, India

Boyapati M. Choudary – Ogene Systems (I) Pvt.Ltd., Hyderabad 500037, India

Thirumalaiswamy Raja – Catalysis and Inorganic Chemistry Division, CSIR-National Chemical Laboratory, Pune 411008, India; orcid.org/0000-0002-2487-7363

Complete contact information is available at:

<https://pubs.acs.org/doi/10.1021/acsomega.2c03555>

Notes

The authors declare no competing financial interest.

■ ACKNOWLEDGMENTS

We acknowledge the Department of Science and Technology, New Delhi, India (IF170386), and the Department of Science and Technology-Science and Engineering Research Board, New Delhi, India (EMR/2016/003195 (Ver-1)), for funds and NEHU, Shillong (SAIF), IIT, Guwahati (CIF), IACS, Kolkata (CSS) for providing instrument facilities.

■ REFERENCES

- (1) Tan, C.; Cao, X.; Wu, X.; He, Q.; Yang, J.; Zhang, X.; Chen, J.; Zhao, W.; Han, S.; Nam, G.; Sindoro, M.; Zhang, H. Recent Advances in Ultrathin Two-Dimensional Nanomaterials. *Chem. Rev.* **2017**, *117*, 6225–6331.
- (2) Cai, Z.; Liu, B.; Zou, X.; Cheng, H. Chemical Vapor Deposition Growth and Applications of Two-Dimensional Materials and Their Heterostructures. *Chem. Rev.* **2018**, *118*, 6091–6133.
- (3) Chen, Y.; Fan, Z.; Zhang, Z.; Niu, W.; Li, C.; Yang, N.; Chen, B.; Zhang, H. Two-Dimensional Metal Nanomaterials: Synthesis, Properties, and Applications. *Chem. Rev.* **2018**, *118*, 6409–6455.
- (4) Wang, Y.; Mao, J.; Meng, X.; Yu, L.; Deng, D.; Bao, X. Catalysis with Two-Dimensional Materials Confining Single Atoms: Concept, Design, and Applications. *Chem. Rev.* **2019**, *119*, 1806–1854.
- (5) Jiang, Y.; Cao, L.; Hu, X.; Ren, Z.; Zhang, C.; Wang, C. Simulating Powder X-Ray Diffraction Patterns of Two-Dimensional Materials. *Inorg. Chem.* **2018**, *57*, 15123–15132.
- (6) Yang, W.; Li, J.; Zhang, X.; Zhang, C.; Jiang, X.; Liu, B. Hydrothermal Approach to Spinel-Type 2D Metal Oxide Nanosheets. *Inorg. Chem.* **2019**, *58*, 549–556.
- (7) Choi, P. G.; Izu, N.; Shirahata, N.; Masuda, Y. SnO₂ Nanosheets for Selective Alkene Gas Sensing. *ACS Appl. Nano Mater.* **2019**, *2*, 1820–1827.
- (8) Masuda, Y.; Ohji, T.; Kato, K. Tin Oxide Nanosheet Assembly for Hydrophobic/Hydrophilic Coating and Cancer Sensing. *ACS Appl. Mater. Interfaces* **2012**, *4*, 1666–1674.
- (9) Liu, Y.; Jiao, Y.; Zhang, Z.; Qu, F.; Umar, A.; Wu, X. Hierarchical SnO₂ Nanostructures Made of Intermingled Ultrathin Nanosheets for Environmental Remediation, Smart Gas Sensor, and Supercapacitor Applications. *ACS Appl. Mater. Interfaces* **2014**, *6*, 2174–2184.
- (10) Xu, X.; Zhuang, J.; Wang, X. SnO₂ Quantum Dots and Quantum Wires: Controllable Synthesis, Self-Assembled 2D Architectures, and Gas-Sensing Properties. *J. Am. Chem. Soc.* **2008**, *130*, 12527–12535.
- (11) Cai, Y.; Xu, J.; Guo, Y.; Liu, J. Ultrathin, Polycrystalline, Two-Dimensional Co₃O₄ for Low-Temperature CO Oxidation. *ACS Catal.* **2019**, *9*, 2558–2567.
- (12) Bai, J.; Han, S.; Peng, R.; Zeng, J.; Jiang, J.; Chen, Y. Ultrathin Rhodium Oxide Nanosheet Nanoassemblies: Synthesis, Morphological Stability, and Electrocatalytic Application. *ACS Appl. Mater. Interfaces* **2017**, *9*, 17195–17200.
- (13) Liang, Z.; Zhang, C.; Xu, Y.; Zhang, W.; Zheng, H.; Cao, R. Dual Tuning of Ultrathin α -Co(OH)₂ Nanosheets by Solvent Engineering and Coordination Competition for Efficient Oxygen Evolution. *ACS Sustainable Chem. Eng.* **2019**, *7*, 3527–3535.
- (14) Rafique, R.; Baek, S. H.; Park, C. Y.; Chang, S.; Gul, A. R.; Ha, S.; Nguyen, T. P.; Oh, H.; Ham, S.; Arshad, M.; Lee, H.; Park, T. J. Morphological Evolution of Upconversion Nanoparticles and Their Biomedical Signal Generation. *Sci. Rep.* **2018**, *8*, 17101.
- (15) Lee, Y.; Shin, H.; Chun, S. H.; Lee, J.; Park, W. J.; Baik, J. M.; Yoon, S.; Kim, M. H. Highly Single Crystalline Ir_xRu_{1-x}O₂ Mixed Metal Oxide Nanowires. *J. Phys. Chem. C* **2012**, *116*, 16300–16304.
- (16) D'Olimpio, G.; Nappini, S.; Vorokhta, M.; Lozzi, L.; Genuzio, F.; Menteg, T. O.; Paolucci, V.; Gürbulak, B.; Duman, S.; Ottaviano, L.; Locatelli, A.; Bondino, F.; Boukhalov, D. W.; Politano, A. Enhanced Electrocatalytic Activity in GaSe and InSe Nanosheets: The Role of Surface Oxides. *Adv. Funct. Mater.* **2020**, *30*, No. 2005466.
- (17) Verre, S.; Ombres, L.; Politano, A. Evaluation of the Free-vibration Frequency and the Variation of the Bending Rigidity of

Graphene Nanoplates: The Role of the Shape Geometry and Boundary Conditions. *J. Nanosci. Nanotechnol.* **2017**, *17*, 8827–8834.

(18) Lamuta, C.; Campi, D.; Pagnotta, L.; Dasadia, A.; Cupolillo, A.; Politano, A. Determination of the Mechanical Properties of SnSe, a Novel Layered Semiconductor. *J. Phys. Chem. Solids* **2018**, *116*, 306–312.

(19) D'Olimpio, G.; Genuzio, F.; Mentis, T. O.; Paolucci, V.; Kuo, C. N.; Al Taleb, A.; Lue, C. S.; Torelli, P.; Farias, D.; Locatelli, A.; Boukhalov, D. W.; Cantalini, C.; Politano, A. Charge Redistribution Mechanisms in SnSe₂ Surfaces Exposed to Oxidative and Humid Environments and Their Related Influence on Chemical Sensing. *J. Phys. Chem. Lett.* **2020**, *11*, 9003–9011.

(20) Boukhalov, D. W.; D'Olimpio, G.; Nappini, S.; Ottaviano, L.; Bondino, F.; Politano, A. III–VI and IV–VI van der Waals Semiconductors InSe, GaSe and GeSe: A Suitable Platform for Efficient Electrochemical Water Splitting, Photocatalysis and Chemical Sensing. *Isr. J. Chem.* **2022**, *62*, No. e202100125.

(21) Chun, S. H.; Choi, H.; Kang, M.; Koh, M.; Lee, N. S.; Lee, S. C.; Lee, M.; Lee, Y.; Lee, C.; Kim, M. H. Highly Efficient Electrochemical Responses on Single Crystalline Ruthenium–Vanadium Mixed Metal Oxide Nanowires. *ACS Appl. Mater. Interfaces* **2013**, *5*, 8401–8406.

(22) Smith, K. B.; Tomassone, M. S. Ultrathin Hollow Graphene Oxide Membranes for Use as Nanoparticle Carriers. *Langmuir* **2017**, *33*, 3765–3775.

(23) Bai, J.; Xu, G.; Xing, S.; Zeng, J.; Jiang, J.; Chen, Y. Hydrothermal Synthesis and Catalytic Application of Ultrathin Rhodium Nanosheet Nanoassemblies. *ACS Appl. Mater. Interfaces* **2016**, *8*, 33635–33641.

(24) Yao, K.; Chen, P.; Zhang, Z.; Li, J.; Ai, R.; Ma, H.; Zhao, B.; Sun, G.; Wu, R.; Tang, X.; Li, B.; Hu, J.; Duan, X.; Duan, X. Synthesis of Ultrathin Two-Dimensional Nanosheets and van der Waals Heterostructures from Non-Layered γ -CuI. *npj 2D Mater. Appl.* **2018**, *2*, 16.

(25) Luo, Y. H.; Chen, C.; Lu, G. W.; Hong, D. L.; He, X. T.; Wang, C.; Wang, J.; Sun, B. Atomically Thin Two-Dimensional Nanosheets with Tunable Spin-Crossover Properties. *J. Phys. Chem. Lett.* **2018**, *9*, 7052–7058.

(26) Paolucci, V.; D'Olimpio, G.; Kuo, C. N.; Lue, C. S.; Boukhalov, D. W.; Cantalini, C.; Politano, A. Self-assembled SnO₂/SnSe₂ Heterostructures: A Suitable Platform for Ultrasensitive NO₂ and H₂ Sensing. *ACS Appl. Mater. Interfaces* **2020**, *12*, 34362–34369.

(27) Boukhalov, D. W.; Marchionni, A.; Filippi, J.; Kuo, C. N.; Fujii, J.; Edla, R.; Nappini, S.; D'Olimpio, G.; Ottaviano, L.; Lue, C. S.; Torelli, P.; Vizza, F.; Politano, A. Efficient Hydrogen Evolution Reaction with Platinum Stannide PtSn₄ via Surface Oxidation. *J. Mater. Chem. A* **2020**, *8*, 2349–2355.

(28) Boukhalov, D. W.; Kuo, C. N.; Nappini, S.; Marchionni, A.; D'Olimpio, G.; Filippi, J.; Mauri, S.; Torelli, P.; Lue, C. S.; Vizza, F.; Politano, A. Efficient Electrochemical Water Splitting with PdSn₄ Dirac Nodal Arc Semimetal. *ACS Catal.* **2021**, *11*, 7311–7318.

(29) Boukhalov, D. W.; Paolucci, V.; D'Olimpio, G.; Cantalini, C.; Politano, A. Chemical Reactions on Surfaces for Applications in Catalysis, Gas Sensing, Adsorption-assisted Desalination and Li-ion Batteries: Opportunities and Challenges for Surface Science. *Phys. Chem. Chem. Phys.* **2021**, *23*, 7541–7552.

(30) Chen, Z.; Lai, J. K. L.; Shek, C. H. Facile Strategy and Mechanism for Orthorhombic SnO₂ Thin Films. *Appl. Phys. Lett.* **2006**, *89*, 231902.

(31) Wittkamper, J.; Xu, Z.; Kombaiah, B.; Ram, F.; De Graef, M.; Kitchin, J. R.; Rohrer, G. S.; Salvador, P. A. Competitive Growth of Scrutinyite (α -PbO₂) and Rutile Polymorphs of SnO₂ on All Orientations of Columbite CoNb₂O₆ Substrates. *Cryst. Growth Des.* **2017**, *17*, 3929–3939.

(32) Bae, J.; Park, J.; Kim, H. Y.; Kim, H.; Park, J. Facile Route to the Controlled Synthesis of Tetragonal and Orthorhombic SnO₂ Films by Mist Chemical Vapor Deposition. *ACS Appl. Mater. Interfaces* **2015**, *7*, 12074–12079.

(33) Carvalho, M. H.; Pereira, E. C.; de Oliveira, A. J. A. Orthorhombic SnO₂ Phase Observed Composite (Sn_{1-x}Ce_x)O₂ Synthesized by Sol–Gel Route. *RSC Adv.* **2018**, *8*, 3958–3963.

(34) Li, X.; Qu, Y. Morphology Evolution of Tin-Based Oxide Hierarchical Structures Synthesized by Molten Salt Approach and Their Applications as Anode for Lithium Ion Battery. *Cryst. Growth Des.* **2016**, *16*, 34–41.

(35) Wang, X.; Xiao, L.; Peng, H.; Liu, W.; Xu, X. SnO₂ Nano-Rods with Superior CO Oxidation Performance. *J. Mater. Chem. A* **2014**, *2*, 5616–5619.

(36) Patil, G. E.; Kajale, D. D.; Gaikwad, V. B.; Jain, G. H. Preparation and Characterization of SnO₂ Nanoparticles by Hydrothermal Route. *Int. Nano Lett.* **2012**, *2*, 17.

(37) Kim, W. J.; Lee, S. W.; Sohn, Y. Metallic Sn Spheres and SnO₂@C Core-Shells by Anaerobic and Aerobic Catalytic Ethanol and CO Oxidation Reactions over SnO₂ Nanoparticles. *Sci. Rep.* **2015**, *5*, 13448.

(38) Kong, L.; Ma, J.; Zhu, Z.; Luan, C.; Yu, X.; Yu, Q. Synthesis of Orthorhombic Structure Epitaxial Tin Oxide Film. *Mater. Lett.* **2010**, *64*, 1350–1353.

(39) Lamelas, F. J.; Reid, S. A. Thin-Film Synthesis of the Orthorhombic Phase of SnO₂. *Phys. Rev. B* **1999**, *60*, 9347–9352.

(40) Sartori, G.; Maggi, R. Use of Solid Catalysts in Friedel-Crafts Acylation Reactions. *Chem. Rev.* **2006**, *106*, 1077–1104.

(41) Pandey, G.; Tiwari, S. K.; Singh, B.; Vanka, K.; Jain, S. *p*-Selective (sp²)-C–H Functionalization for an Acylation/Alkylation Reaction Using Organic Photoredox Catalysis. *Chem. Commun.* **2017**, *53*, 12337–12340.

(42) Olah, G. A. *Friedel-Crafts Chemistry*; Wiley: New York, 1973.

(43) Jin, X.; Wang, A.; Cao, H.; Zhang, S.; Wang, L.; Zheng, X.; Zheng, X. A New Efficient Method for the Preparation of Intermediate Aromatic Ketones by Friedel-Crafts Acylation. *Res. Chem. Intermed.* **2018**, *44*, 5521–5530.

(44) Zuidema, D. R.; Williams, S. L.; Wert, K. J.; Bosma, K. J.; Smith, A. L.; Mebane, R. C. Deoxygenation of Aromatic Ketones Using Transfer Hydrogenolysis with Raney Nickel in 2-Propanol. *Synth. Commun.* **2011**, *41*, 2927–2931.

(45) Mu, M.; Fang, W.; Liu, Y.; Chen, L. Iron(III)-Modified Tungstophosphoric Acid Supported on Titania Catalyst: Synthesis, Characterization, and Friedel-Craft Acylation of *m*-Xylene. *Ind. Eng. Chem. Res.* **2015**, *54*, 8893–8899.

(46) Wang, J.; Pang, Y.-B.; Tao, N.; Zeng, R.; Zhao, Y. Nickel-Catalyzed, *para*-Selective, Radical-Based Alkylation of Aromatic Ketones. *Org. Lett.* **2020**, *22*, 854–857.

(47) Zhao, J.; Hughes, C. O.; Toste, F. D. Synthesis of Aromatic Ketones by a Transition Metal-Catalyzed Tandem Sequence. *J. Am. Chem. Soc.* **2006**, *128*, 7436–7437.

(48) Kusumaningsih, T.; Prasetyo, W. E.; Firdaus, M. A Greatly Improved Procedure for the Synthesis of an Antibiotic-Drug Candidate 2,4-Diacetylphloroglucinol over Silica Sulphuric Acid Catalyst: Multivariate Optimisation and Environmental Assessment Protocol Comparison by Metrics. *RSC Adv.* **2020**, *10*, 31824–31837.

(49) Sawant, R. T.; Stevens, M. Y.; Odell, L. R. Microwave-Assisted *aza*-Friedel-Crafts Arylation of *N*-Acylium Ions: Expedient Access to 4-Aryl 3,4-Dihydroquinazolinones. *ACS Omega* **2018**, *3*, 14258–14265.

(50) Schlegel, M.; Schneider, C. Lewis Acid-Catalyzed Friedel-Crafts Reactions toward Highly Versatile, α -Quaternary Oxime Ethers. *Chem. Commun.* **2018**, *54*, 11124–11127.

(51) Firouzabadi, H.; Iranpoor, N.; Nowrouzi, F. Solvent-Free Friedel-Crafts Acylation of Aromatic Compounds with Carboxylic Acids in the Presence of Trifluoroacetic Anhydride and Aluminum Dodecatungstophosphate. *Tetrahedron Lett.* **2003**, *44*, 5343–5345.

(52) Kawada, A.; Mitamura, S.; Kobayashi, S. Ln(OTf)₃–LiClO₄ as Reusable Catalyst System for Friedel-Crafts Acylation. *Chem. Commun.* **1996**, *02*, 183–184.

(53) Bartoli, G.; Bosco, M.; Marcantoni, E.; Massaccesi, M.; Rinaldi, S.; Sambri, L. LiClO₄–Acyl Anhydrides Complexes as Powerful

Acylation Reagents of Aromatic Compounds in Solvent Free Conditions. *Tetrahedron Lett.* **2002**, *43*, 6331–6333.

(54) Fürstner, A.; Voigtländer, D.; Schrader, W.; Giebel, D.; Reetz, M. T. A “Hard/Soft” Mismatch Enables Catalytic Friedel-Crafts Acylations. *Org. Lett.* **2001**, *3*, 417–420.

(55) Kusama, H.; Narasaka, K. Friedel-Crafts Acylation of Arenes Catalyzed by Bromopentacarbonylrhenium(I). *Bull. Chem. Soc. Jpn.* **1995**, *68*, 2379–2383.

(56) Doan, T. L. H.; Dao, T. Q.; Tran, H. N.; Tran, P. H.; Le, T. N. An Efficient Combination of Zr-MOF and Microwave Irradiation in Catalytic Lewis Acid Friedel-Crafts Benzoylation. *Dalton Trans.* **2016**, *45*, 7875–7880.

(57) Motiwala, H. F.; Vekariya, R. H.; Aubé, J. Intramolecular Friedel-Crafts Acylation Reaction Promoted by 1,1,1,3,3,3-Hexafluoro-2-Propanol. *Org. Lett.* **2015**, *17*, 5484–5487.

(58) Reddy, B. M.; Patil, M. K. Organic Syntheses and Transformations Catalyzed by Sulfated Zirconia. *Chem. Rev.* **2009**, *109*, 2185–2208.

(59) Tran, P. H.; Nguyen, T. D. T.; Tu, T. A. T.; Le, T. N. Magnetically Recoverable γ -Fe₂O₃ Nanoparticles as a Highly Active Catalyst for Friedel-Crafts Benzoylation Reaction under Ultrasound Irradiation. *Arab. J. Chem.* **2020**, *13*, 290–297.

(60) Liu, E.; Locke, A. J.; Frost, R. L.; Martens, W. N. Sulfated Fibrous ZrO₂/Al₂O₃ Core and Shell Nanocomposites: A Novel Strong Acid Catalyst with Hierarchically Macro-Mesoporous Nanostructure. *J. Mol. Catal. A: Chem.* **2012**, *353–354*, 95–105.

(61) Hua, W.; Xia, Y.; Yue, Y.; Gao, Z. Promoting Effect of Al on SO₄²⁻/M_xO_y (M = Zr, Ti, Fe) Catalysts. *J. Catal.* **2000**, *196*, 104–114.

(62) Rao, X.; Ishitani, H.; Yoo, W.-J.; Kobayashi, S. Zirconium- β Zeolite-Catalyzed Continuous-Flow Friedel-Crafts Acylation Reaction. *Asian J. Org. Chem.* **2019**, *8*, 316–319.

(63) Cornélias, A.; Gerstmans, A.; Laszlo, P.; Mathy, A.; Zieba, I. Friedel-Crafts Acylations with Modified Clays as Catalysts. *Catal. Lett.* **1990**, *6*, 103–109.

(64) Sarvari, M. H.; Sharghi, H. Reactions on a Solid Surface. A Simple, Economical and Efficient Friedel-Crafts Acylation Reaction over Zinc Oxide (ZnO) as a New Catalyst. *J. Org. Chem.* **2004**, *69*, 6953–6956.

(65) Yadav, G. D.; Yadav, A. R. Selectivity Engineered Friedel-Crafts Acylation of Guaiacol with Vinyl Acetate to Acetovanillone over Cesium-Modified Heteropolyacid Supported on K-10 Clay. *Ind. Eng. Chem. Res.* **2013**, *52*, 10627–10636.

(66) Martínez, F.; Morales, G.; Martín, A.; van Grieken, R. Perfluorinated Nafion-Modified SBA-15 Materials for Catalytic Acylation of Anisole. *Appl. Catal. A Gen.* **2008**, *347*, 169–178.

(67) Chavali, M. S.; Nikolova, M. P. Metal Oxide Nanoparticles and Their Applications in Nanotechnology. *SN Appl. Sci.* **2019**, *1*, 607.

(68) Pla, D.; Gómez, M. Metal and Metal Oxide Nanoparticles: A Lever for C–H Functionalization. *ACS Catal.* **2016**, *6*, 3537–3552.

(69) Gadipelly, C.; Mannepalli, L. K. Nano-Metal Oxides for Organic Transformations. *Curr. Opin. Green Sustain. Chem.* **2019**, *15*, 20–26.

(70) Desai, D. S.; Yadav, G. D. Friedel-Crafts Acylation of Furan Using Chromium-Exchanged Dodecatungstophosphoric Acid: Effect of Support, Mechanism and Kinetic Modelling. *Clean Technol. Environ. Policy* **2021**, *23*, 2429–2441.

(71) Pimerzin, A. A.; Roganov, A. A.; Verevkin, S. P.; Konnova, M. E.; Pilshchikov, V. A.; Pimerzin, A. A. Bifunctional Catalysts with Noble Metals on Composite Al₂O₃-SAPO-11 Carrier and Their Comparison with CoMoS One in n-Hexadecane Hydroisomerization. *Catal. Today* **2019**, *329*, 71–81.

(72) Yang, X.; Yasukawa, T.; Yamashita, Y.; Kobayashi, S. Development of Trifluoromethanesulfonic Acid-Immobilized Nitrogen-Doped Carbon-Incarcerated Niobia Nanoparticle Catalysts for Friedel-Crafts Acylation. *J. Org. Chem.* **2021**, *86*, 15800–15806.

(73) Du, P.; Zheng, P.; Song, S.; Wang, X.; Zhang, M.; Chi, K.; Xu, C.; Duan, A.; Zhao, Z. Synthesis of a Novel Micro/Mesoporous Composite Material Beta-FDU-12 and Its Hydro-Upgrading Performance for FCC Gasoline. *RSC Adv.* **2016**, *6*, 1018–1026.

(74) Maronna, M. M.; Kruissink, E. C.; Parton, R. F.; Soulimani, F.; Weckhuysen, B. M.; Hoelderich, W. F. Spectroscopic Study on the Active Site of a SiO₂ Supported Niobia Catalyst Used for the Gas-Phase Beckmann Rearrangement of Cyclohexanone Oxime to ϵ -Caprolactam. *Phys. Chem. Chem. Phys.* **2016**, *18*, 22636–22646.

(75) Mokaya, R.; Jones, W. Acidity and Catalytic Activity of Aluminosilicate Mesoporous Molecular Sieves Prepared Using Primary Amines. *Chem. Commun.* **1996**, *8*, 983–985.

(76) Kumari, P. K.; Rao, B. S.; Padmakar, D.; Pasha, N.; Lingaiah, N. Lewis Acidity Induced Heteropoly Tungstate Catalysts for the Synthesis of 5-Ethoxymethyl Furfural from Fructose and 5-Hydroxymethylfurfural. *Mol. Catal.* **2018**, *448*, 108–115.

(77) Cai, M.; Wang, X. Activity of Imidazolium-Based Ionic Liquids as Catalysts for Friedel-Crafts Acylation of Aromatic Compounds. *Asian J. Chem.* **2014**, *26*, 5981–5984.

(78) Ghodke, S. V.; Chudasama, U. V. Friedel-Crafts Alkylation and Acylation of Aromatic Compounds under Solvent-Free Conditions Using Solid Acid Catalysts. *Int. J. Chem. Stud.* **2015**, *2*, 27–34.

(79) Kantam, M. L.; Ranganath, K. V. S.; Sateesh, M.; Kumar, K. B. S.; Choudary, B. M. Friedel-Crafts Acylation of Aromatics and Heteroaromatics by Beta Zeolite. *J. Mol. Catal. A: Chem.* **2005**, *225*, 15–20.

(80) Yamamoto, Y.; Itonaga, K. Versatile Friedel-Crafts-Type Alkylation of Benzene Derivatives Using a Molybdenum Complex/Ortho-Chloranil Catalytic System. *Chem. – Eur. J.* **2008**, *14*, 10705–10715.

(81) Fan, C. M.; Peng, Y.; Zhu, Q.; Lin, L.; Wang, R. X.; Xu, A. W. Synproportionation Reaction for the Fabrication of Sn²⁺ Self-Doped SnO_{2-x} Nanocrystals with Tunable Band Structure and Highly Efficient Visible Light Photocatalytic Activity. *J. Phys. Chem. C* **2013**, *117*, 24157–24166.

(82) Choudhary, V. R.; Jana, S. K. Highly Active and Low Moisture Sensitive Supported Thallium Oxide Catalysts for Friedel-Crafts-Type Benzoylation and Acylation Reactions: Strong Thallium Oxide-Support Interactions. *J. Catal.* **2001**, *201*, 225–235.

(83) Jana, S. K. Advances in Liquid-Phase Friedel-Crafts Acylation of Aromatics Catalyzed by Heterogeneous Solids. *Catal. Surv. Asia* **2006**, *10*, 98–109.

(84) Patil, M. L.; Jnaneshwara, G. K.; Sabde, D. P.; Dongare, M. K.; Sudalai, A.; Deshpande, V. H. Regiospecific Acylations of Aromatics and Selective Reductions of Azobenzenes over Hydrated Zirconia. *Tetrahedron Lett.* **1997**, *38*, 2137–2140.

(85) Mu, M.; Chen, L.; Liu, Y.; Fang, W.; Li, Y. An Efficient Fe₂O₃/HY Catalyst for Friedel-Crafts Acylation of *m*-Xylene with Benzoyl Chloride. *RSC Adv.* **2014**, *4*, 36951–36958.

(86) Rezaei, S. J. T.; Nabid, M. R.; Hosseini, S. Z.; Abedi, M. Polyaniline-Supported Zinc Oxide (ZnO) Nanoparticles: An Active and Stable Heterogeneous Catalyst for the Friedel-Crafts Acylation Reaction. *Synth. Commun.* **2012**, *42*, 1432–1444.

(87) Reddy, K. R.; Venkanna, D.; Kantam, M. L.; Bhargava, S. K.; Srinivasu, P. SnO₂-SiO₂ Mesoporous Composite: A Very Active Catalyst for Regioselective Synthesis of Aromatic Ketones with Unusual Catalytic Behavior. *Ind. Eng. Chem. Res.* **2015**, *54*, 7005–7013.

(88) Pasha, M. A.; Manjula, K.; Jayashankara, V. P. Titanium Dioxide-Mediated Friedel-Crafts Acylation of Aromatic Compounds in Solvent-Free Condition under Microwave Irradiation. *Synth. React. Inorg. Met. Org. Chem.* **2006**, *36*, 321–324.